

Electronic correlations, layer distinction, and electron doping in the alternating single-layer trilayer $\text{La}_3\text{Ni}_2\text{O}_7$ polymorph

Harrison LaBollita,* Soumen Bag, Jesse Kapeghian, and Antia S. Botana
Department of Physics, Arizona State University, Tempe, AZ 85287, USA

We employ a density-functional theory plus dynamical mean-field theory framework to investigate the correlated electronic structure of the alternating single-layer trilayer (1313) polymorph of $\text{La}_3\text{Ni}_2\text{O}_7$ under pressure. At ambient pressure, the single-layer is in a Mott insulating regime and the low-energy physics is dominated by the trilayer block. Under pressure, the gap in the single-layer block closes due to orbital-selective physics, enabling charge transfer into the trilayer block. This change in effective doping of the trilayer block is likely linked to the higher T_c obtained in $\text{La}_3\text{Ni}_2\text{O}_7$ -1313 (~ 80 K) when compared to the nominal trilayer $\text{La}_4\text{Ni}_3\text{O}_{10}$ (~ 30 K). We conclude that correlation-driven layer differentiation is crucial in the $\text{La}_3\text{Ni}_2\text{O}_7$ -1313 polymorph and that its low-energy physics aligns closely with the trilayer $\text{La}_4\text{Ni}_3\text{O}_{10}$ compound (in spite of the apparent differences in nominal filling) rather than with the conventional bilayer $\text{La}_3\text{Ni}_2\text{O}_7$.

I. INTRODUCTION

The discovery of superconductivity in hole-doped infinite-layer nickelates RNiO_2 (R = rare-earth) [1–4] marked the culmination of a multi-decade pursuit for nickelate analogs to the cuprates [5–7]. The subsequent realization of superconductivity in a chemically undoped quintuple-layer nickelate $\text{Nd}_6\text{Ni}_5\text{O}_{12}$ [8] (with a similar $T_c \sim 15$ K) established the first family of nickelate superconductors represented by the general chemical formula $R_{n+1}\text{Ni}_n\text{O}_{2n+2}$ [9–11] ($n = 2, \dots, \infty$). The materials in this family contain n -cuprate-like NiO_2 planes and an average Ni-3d filling that can be tuned with the number of layers (n) corresponding to $d^{9-1/n}$ [12].

The layered nickelates of the $R_{n+1}\text{Ni}_n\text{O}_{2n+2}$ family are derived via oxygen reduction from the parent $R_{n+1}\text{Ni}_n\text{O}_{3n+1}$ Ruddlesden-Popper (RP) compounds which host n -perovskite layers separated by rocksalt R-O spacer layers, with an average Ni-3d filling of $d^{7+1/n}$ [13–17]. Last year, superconductivity was realized under pressure in this parent RP family in bilayer $\text{La}_3\text{Ni}_2\text{O}_7$ with a record $T_c \sim 80$ K at 14 GPa [18–21], as well as in the trilayer $\text{La}_4\text{Ni}_3\text{O}_{10}$ material with a $T_c \sim 30$ K at 20–30 GPa [22–24]. These discoveries revealed a second, albeit related, family of nickelate superconductors that exhibits higher superconducting transition temperatures than their reduced counterparts, stimulating a plethora of experimental [25–28] and theoretical [29–61] work.

Recently, a new polymorph of the bilayer RP phase $\text{La}_3\text{Ni}_2\text{O}_7$ was reported, characterized by a novel stacking sequence where alternating single-layer and trilayer blocks of NiO_6 octahedra form a ‘1313’ configuration [62–64], deviating from the typical uniform bilayer stacking of perovskite blocks (2222). Superconductivity in this new $\text{La}_3\text{Ni}_2\text{O}_7$ -1313 polymorph has also been reported under pressure with a similar T_c to that of the conventional bilayer nickelate $\text{La}_3\text{Ni}_2\text{O}_7$ -2222 [63]. Since $\text{La}_3\text{Ni}_2\text{O}_7$ -1313 combines the single-layer La_2NiO_4 [65, 66] and trilayer

$\text{La}_4\text{Ni}_3\text{O}_{10}$ [67] structures, an important question to answer is whether such a structural superposition extends to the low-energy electronic structure as well.

In this work, we employ a density-functional theory plus dynamical mean-field theory (DFT+DMFT) framework to study the low-energy correlated electronic structure of the $\text{La}_3\text{Ni}_2\text{O}_7$ -1313 polymorph under pressure and analyze its resemblance to the underlying single-layer and trilayer structural constituents. At ambient pressure, a Mott insulating state is obtained in the single-layer block with the low-energy physics being consequently dominated by the trilayer unit. Under pressure, the gap in the single-layer block closes and the trilayer block is effectively electron-doped. This effective doping may be related to the increased superconducting transition temperature of $\text{La}_3\text{Ni}_2\text{O}_7$ -1313 relative to the trilayer RP counterpart $\text{La}_4\text{Ni}_3\text{O}_{10}$. Our findings suggest that a significant correlation-driven layer differentiation is present in $\text{La}_3\text{Ni}_2\text{O}_7$ -1313 and we show that the low-energy correlated physics governing this polymorph aligns more closely with the (electron-doped) trilayer RP phase than with the conventional $\text{La}_3\text{Ni}_2\text{O}_7$ -2222 nickelate.

II. METHODOLOGY

The combination of density-functional theory (DFT) and dynamical mean-field theory (DMFT) was used to study the low-energy correlated electronic structure of $\text{La}_3\text{Ni}_2\text{O}_7$ -1313 and its structural constituents: La_2NiO_4 and $\text{La}_4\text{Ni}_3\text{O}_{10}$. Density-functional theory calculations were performed using the all-electron, full potential code WIEN2k [68]. The correlated space was spanned by the $\text{Ni-}e_g$ $\{d_{x^2-y^2}, d_{z^2}\}$ orbitals in our calculations, which we obtained by downfolding the Kohn-Sham DFT bands onto maximally-localized Wannier functions (MLWFs) [69, 70] corresponding to the $\text{Ni-}e_g$ states. Single-site dynamical mean-field theory calculations were performed using the `solid_dmft` [71] package, built on the TRIQS software library [72]. A continuous-time hybridization expansion (CT-HYB) solver as implemented

* hlabolli@asu.edu

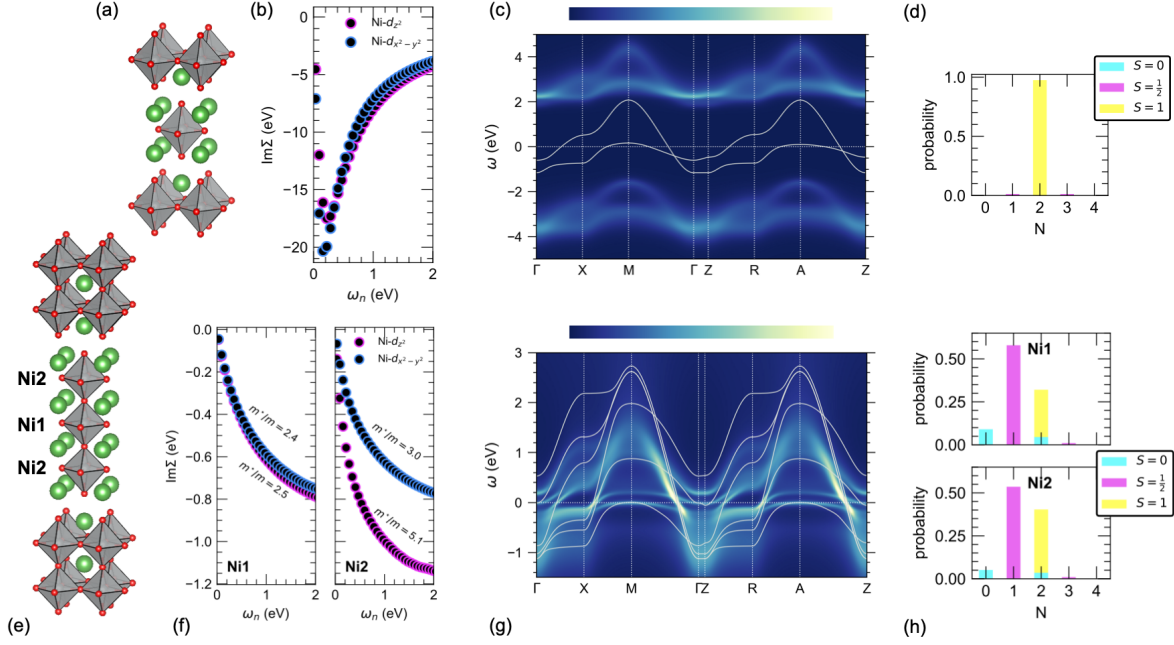


FIG. 1. Crystal structure and correlated low-energy electronic structure of La_2NiO_4 (a-d) and $\text{La}_4\text{Ni}_3\text{O}_{10}$ (e-h) both in a tetragonal $I4/mmm$ structure at ambient pressure ($T = 116$ K). (a) Crystal structure of La_2NiO_4 where green, grey, and red spheres denote La, Ni, and O atoms, respectively. (b) Imaginary part of the Ni- e_g self-energies on the Matsubara axis. (c) \mathbf{k} -resolved spectral function $A(\mathbf{k}, \omega)$. (d) Atomic histogram for the Ni- e_g impurity from the impurity density matrix (measured within the CT-HYB impurity solver) resolved into particle number (N) and spin (S). (e) Crystal structure of $\text{La}_4\text{Ni}_3\text{O}_{10}$ with the two inequivalent Ni sites: inner (Ni1) and outer (Ni2) denoted. (f) Imaginary part of the Ni(1,2)- e_g self-energies on the Matsubara axis (orbital-resolved mass enhancements computed from the low-frequency part inset). (g) \mathbf{k} -resolved spectral function $A(\mathbf{k}, \omega)$. (h) Site-resolved atomic histograms for the Ni- e_g impurities resolved into particle number (N) and spin (S). Solid white lines in (c,g) correspond to the non-interacting bands from DFT.

in TRIQS/cthyb [73] was used to solve the impurity problem(s). Interactions were modeled by a Hubbard-Kanamori Hamiltonian including all spin-flip and pair hopping terms with $U = 5$ eV, $J_H = 1$ eV, and $U' = U - 2J$. All calculations were performed at an inverse electronic temperature corresponding to $\beta = 100$ eV $^{-1}$ and in the paramagnetic state. Instead of full charge self-consistency, our calculations adopt the simpler “one-shot” approach, which has demonstrated success in yielding valuable insights into the correlated physics of various transition-metal oxides [74–77] including nickelates [78–81]. For more details about the calculation settings, see Appendix A.

For consistency and to be able to draw direct comparisons, all the materials were studied within a pseudo-tetragonal crystal setting at ambient pressure, with a $P4/mmm$ structure being used for $\text{La}_3\text{Ni}_2\text{O}_7$ -1313, and an $I4/mmm$ structure for both La_2NiO_4 and $\text{La}_4\text{Ni}_3\text{O}_{10}$. At present, the crystal structure of $\text{La}_3\text{Ni}_2\text{O}_7$ -1313 remains ambiguous, with three potential space groups proposed at ambient pressure: $Cmmm$ (corresponding to a $\sqrt{2} \times \sqrt{2}$ supercell of the tetragonal- $P4/mmm$ parent phase, containing no octahedral tilts) [62, 64], $Imma$ [62], and $Fmmm$ [63] (both exhibiting octahedral tilts). The crystal structure of La_2NiO_4 transitions from

a high-temperature tetragonal ($I4/mmm$) phase to a low-temperature orthorhombic ($Bmab$) phase [66, 82] with only subtle differences in the basic correlated features of their electronic structures [83]. For $\text{La}_4\text{Ni}_3\text{O}_{10}$, the crystal structure has been resolved as monoclinic ($P2_1/a$) or orthorhombic ($Bmab$) at ambient pressure [67], however, previous works [41, 84] have shown that the near Fermi level DFT dispersions of the monoclinic phase can be well reproduced by a $\sqrt{2} \times \sqrt{2}$ tetragonal ($I4/mmm$) structure. The application of pressure tends to ‘tetragonalize’ the crystal structure of all of the materials studied here, as shown before for the $n = 2$ and 3 RP phases [26, 39–41, 63]. Hence, the ambiguity in terms of the space group symmetry is removed in the pressurized phases.

III. RESULTS

Correlated electronic structure of the structural constituents: La_2NiO_4 and $\text{La}_4\text{Ni}_3\text{O}_{10}$.— We start by describing the electronic structure of the two structural constituents of $\text{La}_3\text{Ni}_2\text{O}_7$ -1313, namely, single-layer La_2NiO_4 and trilayer $\text{La}_4\text{Ni}_3\text{O}_{10}$ at ambient pressure. Figure 1 summarizes the key electronic structure features for both materials. The single-layer nickelate La_2NiO_4 (see Fig. 1a) with an average d^8 filling, exhibits metal-

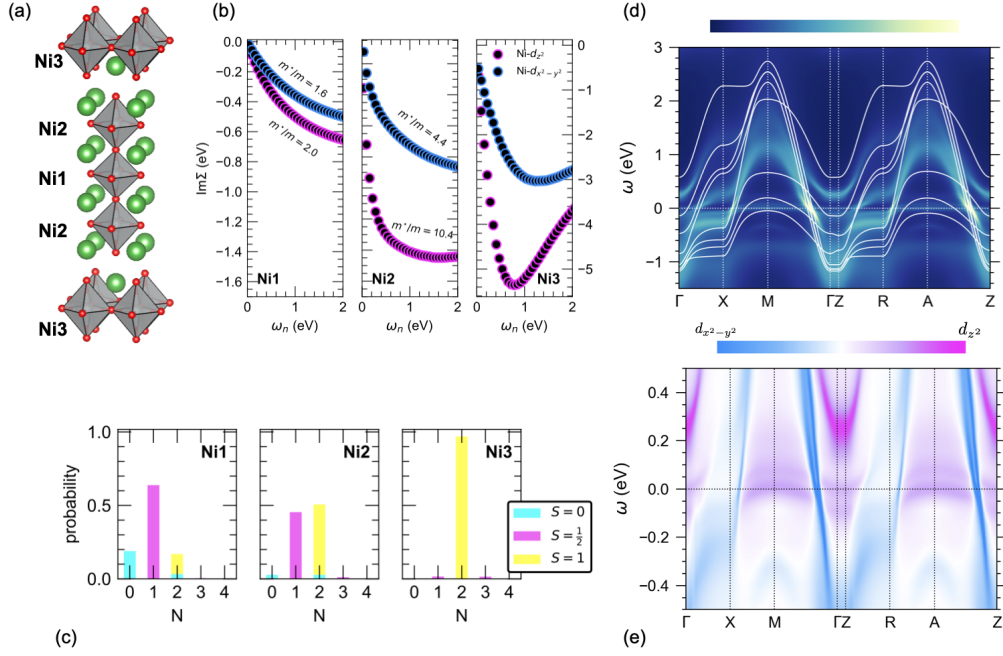


FIG. 2. Crystal structure and correlated low-energy electronic structure of $\text{La}_3\text{Ni}_2\text{O}_7$ -1313 in a tetragonal $P4/mmm$ structure at ambient pressure ($T = 116$ K). (a) Crystal structure of $\text{La}_3\text{Ni}_2\text{O}_7$ -1313 where green, grey, and red spheres denote the La, Ni, and O atoms, respectively, with the three inequivalent Ni sites: inner (Ni1), outer (Ni2), and single-layer (Ni3) denoted. (b) Imaginary part of the $\text{Ni}(1,2,3)\text{-}e_g$ self-energies on the Matsubara axis (orbital-resolved mass enhancements computed from the low-frequency part inset). (c) Site-resolved atomic histograms for the $\text{Ni-}e_g$ impurities obtained from the impurity density matrix (measured within the CT-HYB impurity solver) resolved into particle number (N) and spin (S). (d) \mathbf{k} -resolved spectral function $A(\mathbf{k}, \omega)$. Solid white lines correspond to the non-interacting bands from DFT. (e) Low-energy blow-up of (d) projected onto the $\text{Ni-}e_g$ orbitals. Blue (pink) corresponds to $\text{Ni-}d_{x^2-y^2}$ ($\text{Ni-}d_{z^2}$).

	$n(d_{z^2})$	$n(d_{x^2-y^2})$	n_{total}
La_2NiO_4			
Ni	1.0 (1.0)	1.0 (1.0)	2.0 (2.0)
$\text{La}_4\text{Ni}_3\text{O}_{10}$			
Ni1	0.64 (0.62)	0.61 (0.57)	1.25 (1.19)
Ni2	0.77 (0.77)	0.60 (0.63)	1.37 (1.4)
$\text{La}_3\text{Ni}_2\text{O}_7$ -1313			
Ni1	0.57 (0.62)	0.43 (0.56)	1.0 (1.18)
Ni2	0.86 (0.81)	0.64 (0.63)	1.5 (1.44)
Ni3	1.0 (1.0)	1.0 (0.94)	2.0 (1.94)

TABLE I. Site-resolved $\text{Ni-}e_g$ orbital occupations for La_2NiO_4 , $\text{La}_4\text{Ni}_3\text{O}_{10}$, and $\text{La}_3\text{Ni}_2\text{O}_7$ -1313 at ambient pressure (30 GPa) obtained from the impurity Green's function.

lic behavior at the non-interacting (DFT) level with two bands of $\text{Ni-}e_g$ character crossing the Fermi energy (thin, white lines in Fig. 1c). However, when including local electronic interactions within (single-site) DMFT, La_2NiO_4 transfers into a Mott-insulating regime without the need for antiferromagnetic order (see Fig. 1b), with a gap opening in both orbital sectors evidenced by the local self-energies shown in Fig. 1b. The large (~ 4 eV) gap of this Mott insulating state can be clearly observed

in the \mathbf{k} -summed spectral data (see Fig. 5 of Appendix B) as well as in the \mathbf{k} -resolved spectral function (see Fig. 1c) that is consistent with photoemission data [85], and with previous theoretical calculations [83]. Moreover, this correlated insulating state is characterized by a high-spin ($S = 1$) configuration within the $\text{Ni-}e_g$ manifold (see Fig. 1d) obtained from the impurity density matrix (measured within CT-HYB). This spin configuration corresponds to one electron in each orbital, as expected for a d^8 Ni in an octahedral environment (see Table I for the corresponding orbital occupations derived from the impurity Green's functions).

The trilayer RP nickelate $\text{La}_4\text{Ni}_3\text{O}_{10}$ (see Fig. 1e), with an average $d^{7.33}$ filling, can instead be described as a correlated metal with strong layer-dependent electronic correlations when comparing the inner (Ni1) and outer (Ni2) symmetry inequivalent layers, in agreement with Ref. [59]. These layer-dependent correlations are revealed by the site-resolved local $\text{Ni-}e_g$ self-energies shown in Fig. 1f with the estimated mass enhancements $m^*/m_{\text{DFT}} = (1 - \partial \text{Im}\Sigma / \partial \omega_n)|_{\omega_n \rightarrow 0}$ from the lowest Matsubara frequencies being notably different. On the inner layers (Ni1), correlations are nearly identical in both orbital sectors with $m^*/m_{\text{DFT}} \sim 2.5$. The outer layers (Ni2) show overall significantly stronger electronic correlations with $m^*/m_{\text{DFT}} \sim 5$ for d_{z^2} and $m^*/m_{\text{DFT}} \sim 3$ for

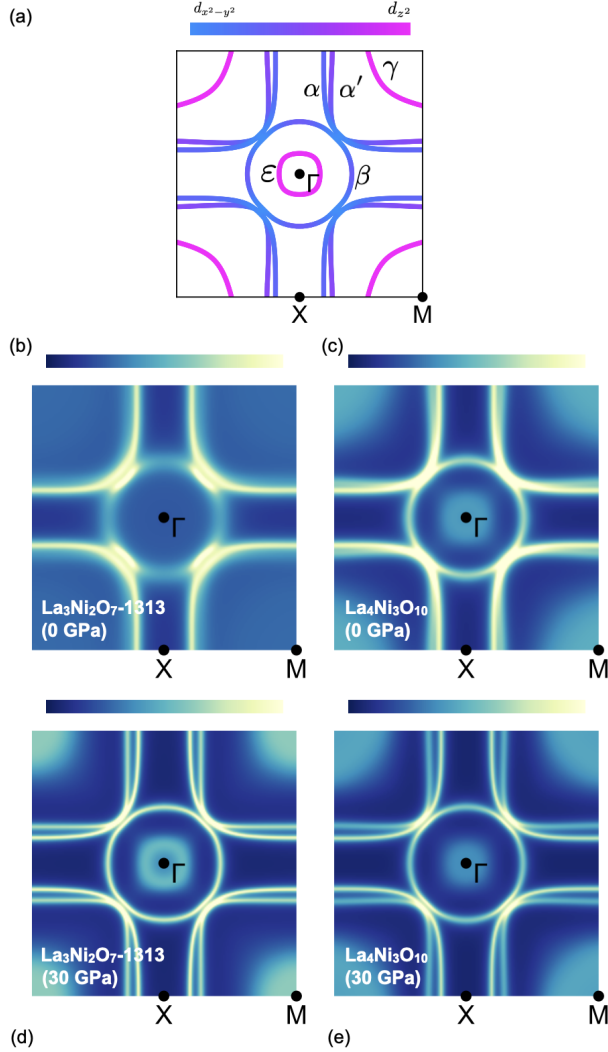


FIG. 3. Schematic of the Fermi surface and interacting Fermi surfaces in the $k_z = 0$ plane for $\text{La}_3\text{Ni}_2\text{O}_7\text{-1313}$ and $\text{La}_4\text{Ni}_3\text{O}_{10}$ (a) Schematic fermiology for $\text{La}_3\text{Ni}_2\text{O}_7\text{-1313}$ and $\text{La}_4\text{Ni}_3\text{O}_{10}$ highlighting the possible Fermi surface sheets with $\text{Ni-}e_g$ orbital character denoted. Lowercase Greek letters are used to label the different sheets. The orbital character is highlighted where blue (pink) corresponds to $\text{Ni-}d_{x^2-y^2}$ ($\text{Ni-}d_{z^2}$) orbital weight. (b,c) Interacting Fermi surfaces ($T = 116$ K) at ambient pressure and (d,e) at 30 GPa for $\text{La}_3\text{Ni}_2\text{O}_7\text{-1313}$ and $\text{La}_4\text{Ni}_3\text{O}_{10}$, respectively.

the $d_{x^2-y^2}$ orbitals. Averaging mass enhancements (over layers and orbitals) gives a value of ~ 3 , which is in agreement with estimated mass enhancements from angle-resolved photoemission spectroscopy (ARPES) data for $\text{La}_4\text{Ni}_3\text{O}_{10}$ [86]. The layer differentiation described above can be connected to the differences in orbital occupations between the two layers derived from the impurity Green's functions (see Table I). The filling of the $\text{Ni-}d_{x^2-y^2}$ orbitals is nearly identical on the two layers, while for the d_{z^2} orbitals Ni2 (outer) is closer to half-filling (with $n_{d_{z^2}} = 0.77$) than Ni1 (inner), with $n_{d_{z^2}} = 0.64$. The to-

tal layer-resolved occupations for Ni1 (inner), Ni2 (outer) read: $n = 1.25, 1.37$, respectively. These differences in occupations result in differences in the preferred atomic configurations where the inner layer disfavors a high-spin state (see Fig. 1h). Albeit subtle in our calculations, this tendency to penalize a high-spin state in the inner layer is in line with the experimentally observed spin density-wave state [87], consistent with non-magnetic inner layers and magnetic outer layers (such a state has also been described theoretically within DFT+ U [41] and RPA-based calculations [60]). The \mathbf{k} -resolved spectral function in Fig. 1g together with the \mathbf{k} -summed spectral data in Fig. 5 of Appendix B show that the low-energy physics is dominated by the $\text{Ni-}e_g$ states with strong orbital mixing. The non-interacting DFT dispersions (thin, white lines in Fig. 1g) appear strongly renormalized due to correlations. Specifically, flat band features of mostly $\text{Ni-}d_{z^2}$ character from both layers flank the chemical potential from above and below with the remaining near chemical potential spectral weight exhibiting $\text{Ni-}d_{x^2-y^2}$ character. The main features that we just described for the correlated electronic structure of $\text{La}_4\text{Ni}_3\text{O}_{10}$ in a tetragonal $I4/mmm$ phase remain in the monoclinic $P2_1/a$ structure as shown in Fig. 6 of Appendix C.

Correlated electronic structure of the $\text{La}_3\text{Ni}_2\text{O}_7\text{-1313}$ polymorph.— We now turn to the low-energy correlated electronic structure of $\text{La}_3\text{Ni}_2\text{O}_7\text{-1313}$ (with an average $d^{7.5}$ filling) at ambient pressure, which is summarized in Fig. 2. As explained above, the structure of $\text{La}_3\text{Ni}_2\text{O}_7\text{-1313}$ is a structural superposition of the single-layer and trilayer nickelates stacked along the c -axis (see Fig. 2a) [62, 63]. This structural amalgam renders three inequivalent Ni sites: Ni1 and Ni2 in the inner and outer layers of the trilayer, respectively, and Ni3 in the single-layer block. Overall, the main features of the correlated electronic structure for $\text{La}_3\text{Ni}_2\text{O}_7\text{-1313}$ can be easily traced to its underlying structural counterparts described in the previous section. Starting with the single-layer, we find that it is in a Mott-insulating regime (with gaps in both orbital sectors), as shown in Fig. 2b, with one electron in each orbital (see Table I). This gives rise to a high-spin ($S = 1$) configuration as shown in Fig. 2c, which is in agreement with previous calculations [88]. As the single-layer is in this Mott insulating regime, the low-energy physics of $\text{La}_3\text{Ni}_2\text{O}_7\text{-1313}$ is subsequently dominated by the trilayer block. Within the trilayer, both layers can be described as correlated metals with correlations being stronger on the outer layers (Ni2) than the inner layers (Ni1), identical to the nominal trilayer $\text{La}_4\text{Ni}_3\text{O}_{10}$ RP described above (see Fig. 2b). While the layer-dependence is qualitatively similar to the trilayer, the local $\text{Ni-}e_g$ self-energies shown in Fig. 2b indicate that some quantitative differences exist. For the outer Ni sites (Ni2), the $\text{Ni-}d_{z^2}$ orbital is much more correlated in $\text{La}_3\text{Ni}_2\text{O}_7\text{-1313}$ with a mass renormalization $m^*/m_{\text{DFT}} \sim 10$ indicating that these states are more localized in $\text{La}_3\text{Ni}_2\text{O}_7\text{-1313}$ than in $\text{La}_4\text{Ni}_3\text{O}_{10}$. The intensified correlations on the outer layers of the trilayer

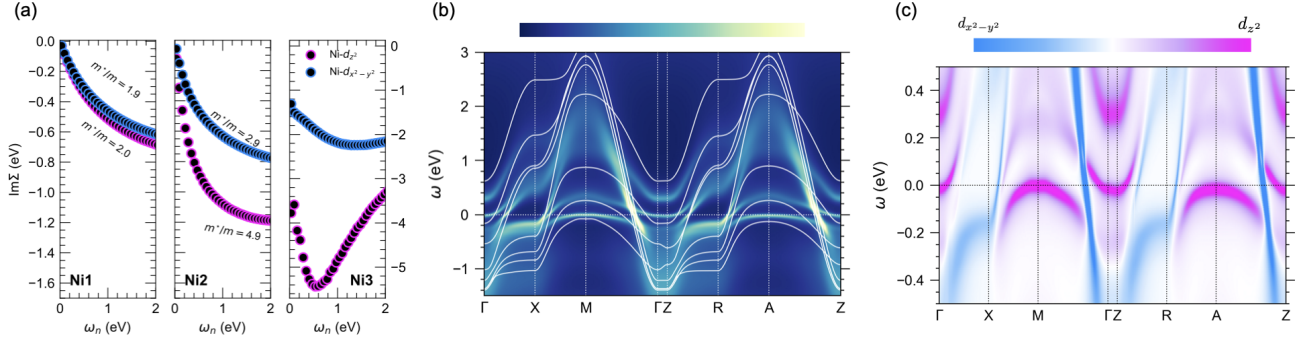


FIG. 4. Correlated low-energy electronic structure of $\text{La}_3\text{Ni}_2\text{O}_7$ -1313 at 30 GPa ($T = 116$ K) for the corresponding DFT-relaxed structure (tetragonal, $P4/mmm$). (a) Imaginary part of the Ni(1,2,3)- e_g self-energies on the Matsubara axis (orbital-resolved mass enhancements computed from the low-frequency part inset). (b) \mathbf{k} -resolved spectral function $A(\mathbf{k}, \omega)$. Solid white lines correspond to the non-interacting (DFT) band structure. (c) Low-energy blow-up of (b) projected onto the Ni- e_g orbitals. Blue (pink) corresponds to $\text{Ni-}d_{x^2-y^2}$ ($\text{Ni-}d_{z^2}$).

can be understood from its proximity to a correlation-driven insulating layer, forcing the Ni2- d_{z^2} states to localize – this feature is absent in $\text{La}_4\text{Ni}_3\text{O}_{10}$. The similar layer-dependence between the individual constituents and $\text{La}_3\text{Ni}_2\text{O}_7$ -1313 is also obvious when comparing the \mathbf{k} -summed spectral data in Fig. 5 of Appendix B. The layer-resolved orbital occupation data in $\text{La}_3\text{Ni}_2\text{O}_7$ -1313 reads: $n = 1$ (Ni1), $n = 1.5$ (Ni2), and $n = 2$ (Ni3) (see Table I). These occupations are expected given the average $\text{Ni}^{2.5+}$ valence for $\text{La}_3\text{Ni}_2\text{O}_7$ -1313 and further highlight the large degree of layer differentiation in this material. The \mathbf{k} -resolved spectral function is shown in Figs. 2d,e. At the non-interacting level, several bands cross the Fermi energy with contributions from all layers and both Ni- e_g orbitals (thin, white lines in Fig. 2d). We find that local interactions significantly renormalize the bare (DFT) band dispersions and redistribute spectral weight away from the chemical potential (particularly, spectral weight from the single-layer block as a consequence of the opening of a Mott gap). A low-energy blow up of the spectral data projected onto the Ni- e_g orbitals in Fig. 2e reveals strongly decoherent Ni- d_{z^2} states around the chemical potential.

Good agreement can be observed when comparing our \mathbf{k} -dependent spectral data to the available ARPES experiments for $\text{La}_3\text{Ni}_2\text{O}_7$ -1313 [89] and $\text{La}_4\text{Ni}_3\text{O}_{10}$ [86], especially when examining the corresponding interacting Fermi surfaces (see Fig. 3). At ambient pressure, the fermiology of both materials is characterized by large hole-like pockets of dominant Ni- $d_{x^2-y^2}$ character (α , α' sheets in the schematic of Fig. 3a) centered at the corner (M) of the Brillouin zone, split due to the inter-layer coupling within the trilayer (see Fig. 3(b,c)). For $\text{La}_4\text{Ni}_3\text{O}_{10}$, a coherent circular electron-like pocket (β) with mixed orbital character is also present, while incoherent spectral weight appears in $\text{La}_3\text{Ni}_2\text{O}_7$ -1313 in this part of the zone. Incoherent spectral weight of Ni- d_{z^2} character is also present in $\text{La}_4\text{Ni}_3\text{O}_{10}$ at the zone corner and zone center (in the position of the γ and ε pockets

in the schematic) due to the strong electronic correlations in this orbital sector. This spectral weight is absent in $\text{La}_3\text{Ni}_2\text{O}_7$ -1313 at ambient pressure. The nearby flat band of d_{z^2} character observed by ARPES [89] below (and close) to the Fermi energy in $\text{La}_3\text{Ni}_2\text{O}_7$ -1313 can also be observed in our spectral data (see Fig. 2e).

We now analyze the evolution of the low-energy correlated electronic structure under pressure. Signatures of superconductivity in $\text{La}_3\text{Ni}_2\text{O}_7$ -1313 emerge above 10 GPa and in $\text{La}_4\text{Ni}_3\text{O}_{10}$ above 20-30 GPa. In order to perform direct comparisons between these two materials, we analyze their electronic structure under pressure using DFT-relaxed structures at 30 GPa which is well within the superconducting regime for both compounds. We focus in the main text on the results for $\text{La}_3\text{Ni}_2\text{O}_7$ -1313 while further details about the correlated electronic structure of the structural constituents at 30 GPa can be found in Figs. 7 and 8 of Appendix D. For pressurized $\text{La}_3\text{Ni}_2\text{O}_7$ -1313, we find that the Mott-insulating nature of the single-layer block at ambient pressure transitions into an orbital-selective Mott state with the Ni- $d_{x^2-y^2}$ orbital exhibiting metallic behavior (see Fig. 4a). Electronic correlations weaken within the trilayer with the outer layers still being the most correlated (see Fig. 4a) with $m^*/m_{\text{DFT}} \sim 2$ for both orbitals on Ni1 (inner) and $m^*/m_{\text{DFT}} \sim 3, 5$ for the Ni- $d_{x^2-y^2}$, d_{z^2} orbitals, respectively, on Ni2 (outer). Both changes in the layer-resolved physics (with respect to ambient pressure) can be understood from the increased electronic bandwidth with pressure, which changes the critical ratio U/t . Interestingly, pressure induces a charge redistribution between the single-layer and trilayer units with charge flowing from the single-layer (Ni3) into the trilayer (Ni1, Ni2). The total occupations on the three distinct layers read: 1.18, 1.44, and 1.94 for Ni1, Ni2, and Ni3, respectively (see Table I). Atomic histograms (not shown) remain qualitatively similar to the ambient pressure case (see Fig. 2c), with only subtle reshuffling of probabilities between different configurations. Overall, the applica-

tion of pressure effectively electron dopes the trilayer block above the nominal filling of $4-e_g$ electrons per trilayer to 4.06 electrons per trilayer, about a 2% doping. This pressure-induced electron doping may have consequences on the superconducting transition temperature of $\text{La}_3\text{Ni}_2\text{O}_7$ -1313 ($T_c \sim 80$ K) relative to $\text{La}_4\text{Ni}_3\text{O}_{10}$ ($T_c \sim 30$ K). Consistent with this observation, previous theoretical calculations for $\text{La}_4\text{Ni}_3\text{O}_{10}$ indeed showed that the superconducting correlations in all leading pairing channels (s^\pm , d_{xy} , $d_{x^2-y^2}$) increase with electron doping [60, 90].

Overall, the \mathbf{k} -dependent spectral data shows that the low-energy physics of pressurized $\text{La}_3\text{Ni}_2\text{O}_7$ -1313 continues to be governed by strongly hybridized $\text{Ni}-e_g$ states with the additional contribution from the metallic single-layer $d_{x^2-y^2}$ orbital. Compared to the ambient pressure case, the $\text{Ni}-d_{z^2}$ bands become much more coherent with sharper ‘flat band-like’ spectral features around the chemical potential (see Figs. 4b,c and Fig. 8 in Appendix D). When looking at the Fermi surface of $\text{La}_3\text{Ni}_2\text{O}_7$ -1313 at 30 GPa (see Fig. 3d) some of the features described above at ambient pressure remain but appear more coherent, in particular the two hole-like pockets of dominant $\text{Ni}-d_{x^2-y^2}$ character around M (α , α'), and the β pocket of mixed orbital character at Γ (analogous to the pressurized $\text{La}_4\text{Ni}_3\text{O}_{10}$ material as shown in Fig. 3e). As the coherence of the $\text{Ni}-d_{z^2}$ states also increases, clear spectral weight can be observed at the zone corner (γ pocket) and zone center (ε pocket) for both materials. Because of the charge-transfer from the single-layer to the trilayer in $\text{La}_3\text{Ni}_2\text{O}_7$ -1313, the effective electron filling within the trilayer is larger than in $\text{La}_4\text{Ni}_3\text{O}_{10}$, which increases the size of the electron-pocket at the zone center and decreases the size of the hole-pockets at the zone corners relative to nominal $\text{La}_4\text{Ni}_3\text{O}_{10}$. Overall, with the above considerations, the interacting fermiology of pressurized $\text{La}_3\text{Ni}_2\text{O}_7$ -1313 can simply be interpreted as electron-doped $\text{La}_4\text{Ni}_3\text{O}_{10}$.

IV. SUMMARY AND DISCUSSION

Our DFT+DMFT calculations for $\text{La}_3\text{Ni}_2\text{O}_7$ -1313 (and its structural constituents La_2NiO_4 and $\text{La}_4\text{Ni}_3\text{O}_{10}$) elucidate several key features concerning the evolution of the correlated electronic structure of this material under pressure. At ambient pressure, the correlated electronic structure of $\text{La}_3\text{Ni}_2\text{O}_7$ -1313 is characterized by distinctly different physics on the three inequivalent layers with a correlated metallic trilayer unit (characterized by variable correlations on the inner and outer layers) sandwiched by a Mott-insulating single-layer. This alternating stack of insulating and metallic layers renders the correlated physics much stronger in the trilayer block of $\text{La}_3\text{Ni}_2\text{O}_7$ -1313 than in the nominal trilayer block in $\text{La}_4\text{Ni}_3\text{O}_{10}$. Pressurizing $\text{La}_3\text{Ni}_2\text{O}_7$ -1313 has interesting consequences on the correlation physics of this material. Orbital-selective physics emerges within the single-layer

with the $\text{Ni}-d_{z^2}$ orbital remaining in a Mott regime, while the $\text{Ni}-d_{x^2-y^2}$ orbital becomes metallic. Furthermore, pressure induces a charge flow from the single-layer to the trilayer, which effectively electron dopes the trilayer unit. In this manner, pressurized $\text{La}_3\text{Ni}_2\text{O}_7$ -1313 can be thought of as electron-doped $\text{La}_4\text{Ni}_3\text{O}_{10}$ when analyzed at the same pressure. This effective electron doping could be connected to the larger superconducting T_c of $\text{La}_3\text{Ni}_2\text{O}_7$ -1313 when compared to $\text{La}_4\text{Ni}_3\text{O}_{10}$. Overall, we conclude that correlation-driven layer differentiation plays a crucial role in the electronic structure of the $\text{La}_3\text{Ni}_2\text{O}_7$ -1313 polymorph, closely aligning its low-energy physics with that of the trilayer $\text{La}_4\text{Ni}_3\text{O}_{10}$. Electron doping $\text{La}_4\text{Ni}_3\text{O}_{10}$ as well as $\text{La}_3\text{Ni}_2\text{O}_7$ -1313 could be a promising route to increase the superconducting T_c of these materials.

Note added. During the completion of this work, a preprint [91] appeared reporting the electronic structure and superconducting instabilities (at the RPA level) in this newly reported $\text{La}_3\text{Ni}_2\text{O}_7$ polymorph.

ACKNOWLEDGEMENTS

The authors acknowledge support from NSF Grant No. DMR-2045826 and NSF Grant No. DMR-2323971, as well as the ASU Research Computing Center for HPC resources.

Appendix A: Structural data and calculation settings

Crystal structure data for La_2NiO_4 ($I4/mmm$), $\text{La}_3\text{Ni}_2\text{O}_7$ -1313 ($P4/mmm$), and $\text{La}_4\text{Ni}_3\text{O}_{10}$ ($P2_1/a$ and $I4/mmm$) at ambient pressure was obtained from Refs. 62, 82, and 84, respectively. The crystal structures under pressure (at 30 GPa) for the three materials were obtained by relaxing the lattice and internal coordinates with an applied external pressure of 30 GPa within the VASP code [92–94] in the nonmagnetic state and with the Perdew-Burke-Ernzerhof (PBE) version [95] of the generalized gradient approximation (GGA) as the exchange-correlation functional. Subsequent density-functional theory calculations within WIEN2k (as described in the main text) were also performed with the Perdew-Burke-Ernzerhof (PBE) version [95] of the generalized gradient approximation as the exchange-correlation functional. The basis set size was set by $RK_{\text{max}} = 7$. Brillouin zone integration was performed on a $21 \times 21 \times 21$ k -grid for La_2NiO_4 ($I4/mmm$) and $\text{La}_4\text{Ni}_3\text{O}_{10}$ ($I4/mmm$), a $30 \times 29 \times 11$ k -grid was used for $\text{La}_4\text{Ni}_3\text{O}_{10}$ ($P2_1/a$), and a $37 \times 37 \times 7$ k -grid for $\text{La}_3\text{Ni}_2\text{O}_7$ ($P4/mmm$).

To construct our quantum impurity problem(s), the Kohn-Sham DFT bands were downfolded onto localized ‘atomic’-like orbitals with e_g $\{d_{z^2}, d_{x^2-y^2}\}$ symmetry, which are representative of the $\text{Ni-}e_g$ states, using maximally localized Wannier functions (MLWFs) as implemented in Wannier90 [69], which is interfaced to WIEN2k via WIEN2WANNIER [70]. The quantum impurity problem(s) (defined by the two-orbital $\text{Ni-}e_g$ space) were solved within single-site DMFT employing the `solid_dmft` package [71] built on top of the TRIQS software library [72], as explained in the main text. The quantum impurity problem(s) were solved using the CT-HYB impurity solver as implemented in TRIQS/cthyb [73] utilizing up to 10^8 cycles to obtain accurate quantum Monte Carlo data. Green’s functions were represented in a basis of Legendre polynomials (with 70 coefficients) leading to a smooth self-energy on the Matsubara axis. All calculations were performed at an inverse electronic temperature of $\beta = 100 \text{ eV}^{-1}$ ($T = 116 \text{ K}$). The “double-counting” term was absorbed into the chemical potential, since we worked only in the low-energy space spanned by the $\text{Ni-}e_g$ -like Wannier orbitals. Real-frequency data was obtained by analytic continuation using the maximum-entropy method for the impurity Green’s functions and self-energies [96].

Appendix B: Additional data for ambient pressure cases

Figure 5 shows the site- and orbital-resolved impurity \mathbf{k} -summed spectral data for La_2NiO_4 , $\text{La}_4\text{Ni}_3\text{O}_{10}$, and $\text{La}_3\text{Ni}_2\text{O}_7$ -1313 at ambient pressure. The similar layer-dependence between $\text{La}_3\text{Ni}_2\text{O}_7$ -1313 and its structural constituents (with some quantitative differences) is ap-

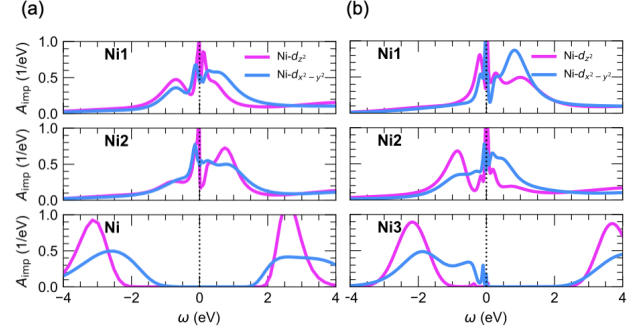


FIG. 5. Site- and orbital ($\text{Ni-}e_g$)-resolved impurity \mathbf{k} -summed spectral data at ambient pressure for (a) La_2NiO_4 (Ni; bottom panel), $\text{La}_4\text{Ni}_3\text{O}_{10}$ (Ni1 and Ni2; top and middle panels), and (b) $\text{La}_3\text{Ni}_2\text{O}_7$ -1313.

parent: within the trilayer the low-energy physics is comprised of strongly hybridized $\text{Ni-}e_g$ states with flat-band like features from the $\text{Ni-}d_{z^2}$ states and notable differences between inner (Ni1) and outer (Ni2) layers. The single layer (Ni/Ni3) is always in a Mott-insulating state.

Appendix C: Correlated electronic structure of ambient pressure $\text{La}_4\text{Ni}_3\text{O}_{10}$ ($P2_1/a$)

Figure 6 summarizes the correlated electronic structure of $\text{La}_4\text{Ni}_3\text{O}_{10}$ in the monoclinic ($P2_1/a$) crystal setting (see Fig 6a). Overall, we find qualitative agreement between the main features of the electronic structure of $\text{La}_4\text{Ni}_3\text{O}_{10}$ in both monoclinic and tetragonal crystal settings (the latter is described in the main text). The \mathbf{k} -resolved spectral data reveals the low-energy physics is comprised of strongly hybridized $\text{Ni-}e_g$ states with flat-band like features from the $\text{Ni-}d_{z^2}$ states (see Fig. 6c). Layer-dependent correlations remain a central correlated feature of $\text{La}_4\text{Ni}_3\text{O}_{10}$ even in the monoclinic setting evidenced by the local $\text{Ni-}e_g$ self-energies (see Fig. 6b). The topology of the Fermi surface shows ‘backfolding’ compared to the tetragonal crystal structure, however, the main spectral features remain the same (see Fig. 6d). The atomic multiplets (not shown) for the impurity problem(s) are qualitatively similar to the tetragonal case (see Fig. 1h in the main text).

Appendix D: Additional data for pressurized ($P = 30 \text{ GPa}$) cases

Figures 7 and 8 show the spectral data and local self-energies for La_2NiO_4 and $\text{La}_4\text{Ni}_3\text{O}_{10}$ at 30 GPa (the structure of both compounds becomes tetragonal under pressure). At 30 GPa, La_2NiO_4 remains in a Mott-insulating state with a $\sim 3 \text{ eV}$ charge gap (see Fig. 7a, and Fig. 8a), however, the “Mottness” is weakened (see Fig. 7b) compared to the ambient pressure case due to the

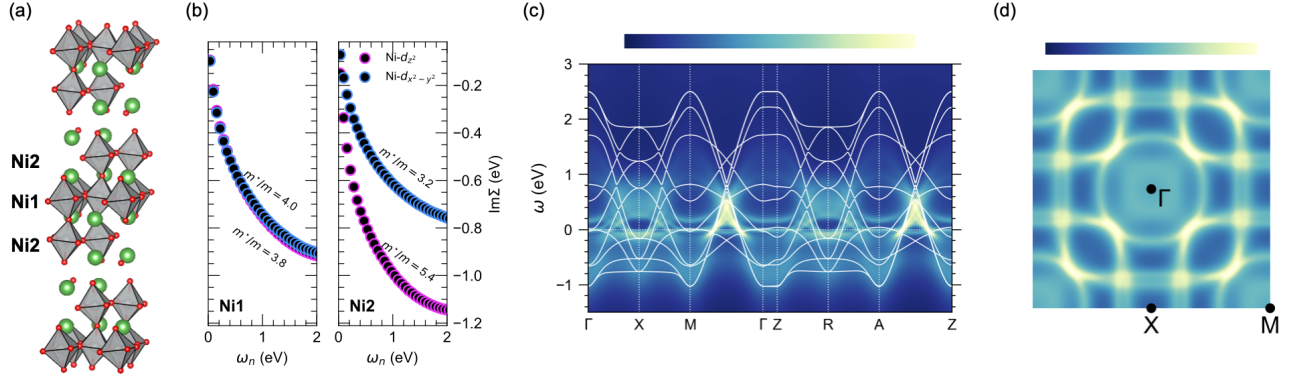


FIG. 6. Structure and correlated low-energy electronic structure of $\text{La}_4\text{Ni}_3\text{O}_{10}$ in a monoclinic $P2_1/a$ setting at ambient pressure ($T = 116$ K). (a) Crystal structure of $\text{La}_4\text{Ni}_3\text{O}_{10}$ with the two inequivalent Ni sites: inner (Ni1) and outer (Ni2) denoted. (b) Imaginary part of the Ni(1,2)- e_g self-energies on the Matsubara axis (orbital-resolved mass enhancements computed from the low-frequency part inset). (c) \mathbf{k} -resolved spectral function $A(\mathbf{k}, \omega)$. Solid white lines correspond to the non-interacting (DFT) band structure. (d) Interacting Fermi surface in the $k_z = 0$ plane.

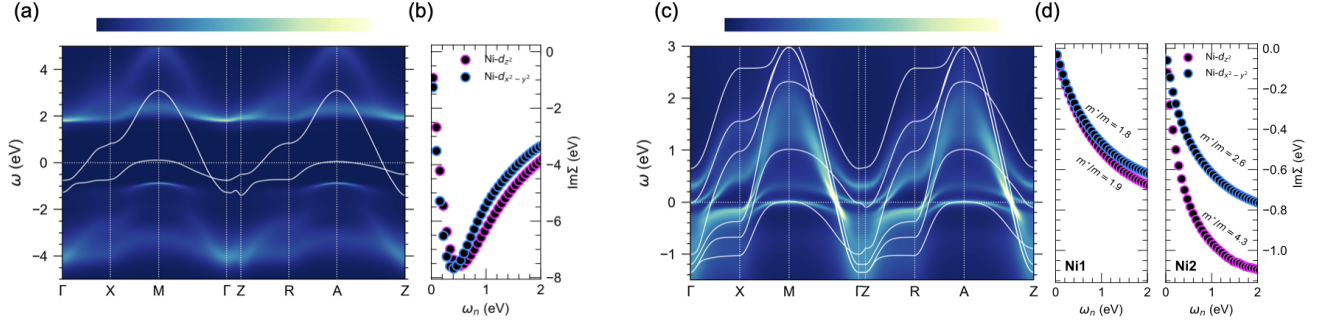


FIG. 7. Correlated low-energy electronic structure of La_2NiO_4 (a-b) and $\text{La}_4\text{Ni}_3\text{O}_{10}$ (c-d) at 30 GPa ($T = 116$ K) using the corresponding DFT-relaxed structures (both tetragonal, $I4/mmm$). (a, c) \mathbf{k} -resolved spectral function $A(\mathbf{k}, \omega)$ for La_2NiO_4 (a) and $\text{La}_4\text{Ni}_3\text{O}_{10}$ (c). Solid white lines correspond to the non-interacting bands from DFT. (b, d) Imaginary part of the Ni- e_g self-energies on the Matsubara axis for La_2NiO_4 (b) and for the two inequivalent Ni atoms in $\text{La}_4\text{Ni}_3\text{O}_{10}$, Ni1 and Ni2 (d) wherein orbital-resolved mass enhancements are computed from the low-frequency part inset.

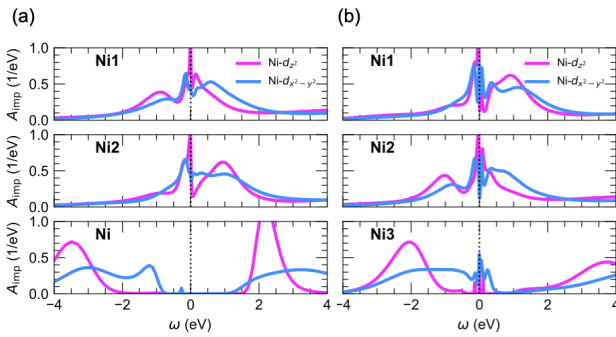


FIG. 8. Site- and orbital (Ni- e_g)-resolved impurity \mathbf{k} -summed spectral data at 30 GPa for (a) La_2NiO_4 (Ni; bottom panel), $\text{La}_4\text{Ni}_3\text{O}_{10}$ (Ni1 and Ni2; top and middle panels), and (b) $\text{La}_3\text{Ni}_2\text{O}_7$ -1313.

increased electronic bandwidth of the Ni- e_g bands. This is different than the pressurized $\text{La}_3\text{Ni}_2\text{O}_7$ -1313 where the single layer exhibits orbital-selective physics as described in the main text (see also Fig. 8b).

The trilayer RP $\text{La}_4\text{Ni}_3\text{O}_{10}$ at 30 GPa remains a correlated metal with layer-dependent correlations (see Fig. 7c and Fig. 8a). Pressure increases the bandwidth of the Ni- e_g bands, which decreases the electronic correlations on both layers (see Fig. 7d). The inner (Ni1) layers always exhibit weaker correlations, than the outer (Ni2) layers in connection to the different orbital fillings between the two layers (see Table I).

[1] D. Li, K. Lee, B. Y. Wang, M. Osada, S. Crossley, H. R. Lee, Y. Cui, Y. Hikita, and H. Y. Hwang, Supercon-

ductivity in an infinite-layer nickelate, *Nature* **572**, 624

- (2019).
- [2] M. Osada, B. Y. Wang, B. H. Goodge, K. Lee, H. Yoon, K. Sakuma, D. Li, M. Miura, L. F. Kourkoutis, and H. Y. Hwang, A superconducting praseodymium nickelate with infinite layer structure, *Nano Letters* **20**, 5735 (2020).
 - [3] M. Osada, B. Y. Wang, B. H. Goodge, S. P. Harvey, K. Lee, D. Li, L. F. Kourkoutis, and H. Y. Hwang, Nickelate superconductivity without rare-earth magnetism: (La,Sr)NiO₂, *Adv. Mater.* **33**, 2104083 (2021).
 - [4] S. Zeng, C. Li, L. E. Chow, Y. Cao, Z. Zhang, C. S. Tang, X. Yin, Z. S. Lim, J. Hu, P. Yang, and A. Ariando, Superconductivity in infinite-layer nickelate La_{1-x}Ca_xNiO₂ thin films, *Sci Adv* **8**, eabl9927 (2022).
 - [5] B. Keimer, S. A. Kivelson, M. R. Norman, S. Uchida, and J. Zaanen, From quantum matter to high-temperature superconductivity in copper oxides, *Nature* **518**, 179 (2015).
 - [6] V. I. Anisimov, D. Bukhvalov, and T. M. Rice, Electronic structure of possible nickelate analogs to the cuprates, *Phys. Rev. B* **59**, 7901 (1999).
 - [7] K.-W. Lee and W. E. Pickett, Infinite-layer LaNiO₂: Ni¹⁺ is not Cu²⁺, *Phys. Rev. B* **70**, 165109 (2004).
 - [8] G. A. Pan, D. Ferenc Segedin, H. LaBollita, Q. Song, E. M. Nica, B. H. Goodge, A. T. Pierce, S. Doyle, S. Novakov, D. Córdoba Carrizales, A. T. N'Diaye, P. Shafer, H. Paik, J. T. Heron, J. A. Mason, A. Yacoby, L. F. Kourkoutis, O. Erten, C. M. Brooks, A. S. Botana, and J. A. Mundy, Superconductivity in a quintuple-layer square-planar nickelate, *Nat. Mater.* **21**, 160 (2022).
 - [9] P. Lacorre, Passage from T'-type to T'-type arrangement by reducing R₄Ni₃O₁₀ to R₄Ni₃O₈ (R = La, Pr, Nd), *J. Solid State Chem.* **97**, 495 (1992).
 - [10] V. V. Poltavets, K. A. Lokshin, S. Dikmen, M. Croft, T. Egami, and M. Greenblatt, La₃Ni₂O₆: A new double T'-type nickelate with infinite Ni^{1+/2+}O₂ layers, *J. Am. Chem. Soc.* **128**, 9050 (2006).
 - [11] V. V. Poltavets, K. A. Lokshin, M. Croft, T. K. Mandal, T. Egami, and M. Greenblatt, Crystal structures of Ln₄Ni₃O₈ (Ln = La, Nd) triple layer T'-type nickelates, *Inorg. Chem.* **46**, 10887 (2007).
 - [12] H. LaBollita and A. S. Botana, Electronic structure and magnetic properties of higher-order layered nickelates: La_{n+1}Ni_nO_{2n+2} (n = 4-6), *Phys. Rev. B* **104**, 035148 (2021).
 - [13] M. Greenblatt, Ruddlesden-popper Ln_{n+1}Ni_nO_{3n+1} nickelates: structure and properties, *Curr. Opin. Solid State Mater. Sci.* **2**, 174 (1997).
 - [14] C. D. Ling, D. N. Argyriou, G. Wu, and J. Neumeier, Neutron diffraction study of La₃Ni₂O₇: Structural relationships among n = 1, 2, and 3 phases La_{n+1}Ni_nO_{3n+1}, *J. Solid State Chem.* **152**, 517 (2000).
 - [15] Z. Li, W. Guo, T. T. Zhang, J. H. Song, T. Y. Gao, Z. B. Gu, and Y. F. Nie, Epitaxial growth and electronic structure of Ruddlesden-Popper nickelates (La_{n+1}Ni_nO_{3n+1}, n = 1-5), *APL Materials* **8**, 091112 (2020).
 - [16] Q. Lei, M. Golalikhani, B. A. Davidson, G. Liu, D. G. Schlom, Q. Qiao, Y. Zhu, R. U. Chandrasena, W. Yang, A. X. Gray, E. Arenholz, A. K. Farrar, D. A. Tenne, M. Hu, J. Guo, R. K. Singh, and X. Xi, Constructing oxide interfaces and heterostructures by atomic layer-by-layer laser molecular beam epitaxy, *npj Quantum Mater.* **2**, 10 (2017).
 - [17] G. A. Pan, Q. Song, D. Ferenc Segedin, M.-C. Jung, H. El-Sherif, E. E. Fleck, B. H. Goodge, S. Doyle, D. Córdoba Carrizales, A. T. N'Diaye, P. Shafer, H. Paik, L. F. Kourkoutis, I. El Baggari, A. S. Botana, C. M. Brooks, and J. A. Mundy, Synthesis and electronic properties of Nd_{n+1}Ni_nO_{3n+1} Ruddlesden-Popper nickelate thin films, *Phys. Rev. Mater.* **6**, 055003 (2022).
 - [18] H. Sun, M. Huo, X. Hu, J. Li, Z. Liu, Y. Han, L. Tang, Z. Mao, P. Yang, B. Wang, J. Cheng, D.-X. Yao, G.-M. Zhang, and M. Wang, Signatures of superconductivity near 80 K in a nickelate under high pressure, *Nature* **621**, 493 (2023).
 - [19] Y. Zhang, D. Su, Y. Huang, H. Sun, M. Huo, Z. Shan, K. Ye, Z. Yang, R. Li, M. Smidman, M. Wang, L. Jiao, and H. Yuan, High-temperature superconductivity with zero-resistance and strange metal behavior in La₃Ni₂O₇, *arXiv:2307.14819* (2023).
 - [20] J. Hou, P.-T. Yang, Z.-Y. Liu, J.-Y. Li, P.-F. Shan, L. Ma, G. Wang, N.-N. Wang, H.-Z. Guo, J.-P. Sun, Y. Uwatoko, M. Wang, G.-M. Zhang, B.-S. Wang, and J.-G. Cheng, Emergence of high-temperature superconducting phase in pressurized La₃Ni₂O₇ crystals, *Chin. Phys. Lett.* **40**, 117302 (2023).
 - [21] J. Li, P. Ma, H. Zhang, X. Huang, C. Huang, M. Huo, D. Hu, Z. Dong, C. He, J. Liao, X. Chen, T. Xie, H. Sun, and M. Wang, Pressure-driven right-triangle shape superconductivity in bilayer nickelate La₃Ni₂O₇, *arXiv:2404.11369* (2024).
 - [22] Q. Li, Y.-J. Zhang, Z.-N. Xiang, Y. Zhang, X. Zhu, and H.-H. Wen, Signature of superconductivity in pressurized La₄Ni₃O₁₀, *Chin. Phys. Lett.* **41**, 017401 (2024).
 - [23] M. Zhang, C. Pei, X. Du, Y. Cao, Q. Wang, J. Wu, Y. Li, Y. Zhao, C. Li, W. Cao, S. Zhu, Q. Zhang, N. Yu, P. Cheng, J. Zhao, Y. Chen, H. Guo, L. Yang, and Y. Qi, Superconductivity in trilayer nickelate La₄Ni₃O₁₀ under pressure, *arXiv:2311.07423* (2023).
 - [24] Y. Zhu, E. Zhang, B. Pan, X. Chen, D. Peng, L. Chen, H. Ren, F. Liu, N. Li, Z. Xing, J. Han, J. Wang, D. Jia, H. Wo, Y. Gu, Y. Gu, L. Ji, W. Wang, H. Gou, Y. Shen, T. Ying, X. Chen, W. Yang, C. Zheng, Q. Zeng, J.-G. Guo, and J. Zhao, Superconductivity in trilayer nickelate La₄Ni₃O₁₀ single crystals, *arXiv:2311.07353* (2024).
 - [25] G. Wang, N. N. Wang, X. L. Shen, J. Hou, L. Ma, L. F. Shi, Z. A. Ren, Y. D. Gu, H. M. Ma, P. T. Yang, Z. Y. Liu, H. Z. Guo, J. P. Sun, G. M. Zhang, S. Calder, J.-Q. Yan, B. S. Wang, Y. Uwatoko, and J.-G. Cheng, Pressure-induced superconductivity in polycrystalline La₃Ni₂O_{7-δ}, *Phys. Rev. X* **14**, 011040 (2024).
 - [26] L. Wang, Y. Li, S.-Y. Xie, F. Liu, H. Sun, C. Huang, Y. Gao, T. Nakagawa, B. Fu, B. Dong, Z. Cao, R. Yu, S. I. Kawaguchi, H. Kadobayashi, M. Wang, C. Jin, H.-k. Mao, and H. Liu, Structure responsible for the superconducting state in La₃Ni₂O₇ at high-pressure and low-temperature conditions, *J. Am. Chem. Soc.* **146**, 7506 (2024).
 - [27] Y. Zhou, J. Guo, S. Cai, H. Sun, P. Wang, J. Zhao, J. Han, X. Chen, Q. Wu, Y. Ding, M. Wang, T. Xiang, H. Kwang Mao, and L. Sun, Evidence of filamentary superconductivity in pressurized La₃Ni₂O₇ single crystals, *arXiv:2311.12361* (2023).
 - [28] F. Li, N. Guo, Q. Zheng, Y. Shen, S. Wang, Q. Cui, C. Liu, S. Wang, X. Tao, G.-M. Zhang, and J. Zhang, Design and synthesis of three-dimensional hybrid Ruddlesden-Popper nickelate single crystals, *arXiv:2312.08116* (2023).
 - [29] Y. Zhang, L.-F. Lin, A. Moreo, and E. Dagotto, Elec-

- tronic structure, dimer physics, orbital-selective behavior, and magnetic tendencies in the bilayer nickelate superconductor $\text{La}_3\text{Ni}_2\text{O}_7$ under pressure, *Phys. Rev. B* **108**, L180510 (2023).
- [30] Y. Gu, C. Le, Z. Yang, X. Wu, and J. Hu, Effective model and pairing tendency in bilayer Ni-based superconductor $\text{La}_3\text{Ni}_2\text{O}_7$, *arXiv:2306.07275* (2023).
- [31] X. Chen, P. Jiang, J. Li, Z. Zhong, and Y. Lu, Critical charge and spin instabilities in superconducting $\text{La}_3\text{Ni}_2\text{O}_7$, *arXiv:2307.07154* (2023).
- [32] F. Lechermann, J. Gondolf, S. Bötzel, and I. M. Eremin, Electronic correlations and superconducting instability in $\text{La}_3\text{Ni}_2\text{O}_7$ under high pressure, *Phys. Rev. B* **108**, L201121 (2023).
- [33] V. Christiansson, F. Petocchi, and P. Werner, Correlated electronic structure of $\text{La}_3\text{Ni}_2\text{O}_7$ under pressure, *Phys. Rev. Lett.* **131**, 206501 (2023).
- [34] Z. Luo, X. Hu, M. Wang, W. Wú, and D.-X. Yao, Bilayer two-orbital model of $\text{La}_3\text{Ni}_2\text{O}_7$ under pressure, *Phys. Rev. Lett.* **131**, 126001 (2023).
- [35] Y. Shen, M. Qin, and G.-M. Zhang, Effective bilayer model hamiltonian and density-matrix renormalization group study for the high- T_c superconductivity in $\text{La}_3\text{Ni}_2\text{O}_7$ under high pressure, *Chin. Phys. Lett.* **40**, 127401 (2023).
- [36] Q.-G. Yang, D. Wang, and Q.-H. Wang, Possible s_{\pm} -wave superconductivity in $\text{La}_3\text{Ni}_2\text{O}_7$, *Phys. Rev. B* **108**, L140505 (2023).
- [37] Y.-B. Liu, J.-W. Mei, F. Ye, W.-Q. Chen, and F. Yang, s_{\pm} -wave pairing and the destructive role of apical-oxygen deficiencies in $\text{La}_3\text{Ni}_2\text{O}_7$ under pressure, *Phys. Rev. Lett.* **131**, 236002 (2023).
- [38] Y. Zhang, L.-F. Lin, A. Moreo, T. A. Maier, and E. Dagotto, Structural phase transition, s_{\pm} -wave pairing, and magnetic stripe order in bilayered superconductor $\text{La}_3\text{Ni}_2\text{O}_7$ under pressure, *Nat. Commun* **15**, 2470 (2024).
- [39] B. Geisler, J. J. Hamlin, G. R. Stewart, R. G. Hennig, and P. Hirschfeld, Structural transitions, octahedral rotations, and electronic properties of $\text{A}_3\text{Ni}_2\text{O}_7$ rare-earth nickelates under high pressure, *npj Quantum Mater.* **9** (2024).
- [40] H. LaBollita, V. Pardo, M. R. Norman, and A. S. Botana, Electronic structure and magnetic properties of $\text{La}_3\text{Ni}_2\text{O}_7$ under pressure, *arXiv:2309.17279* (2023).
- [41] H. LaBollita, J. Kapeghian, M. R. Norman, and A. S. Botana, Electronic structure and magnetic tendencies of trilayer $\text{La}_4\text{Ni}_3\text{O}_{10}$ under pressure: structural transition, molecular orbitals, and layer differentiation, *arXiv:2402.05085* (2024).
- [42] X.-Z. Qu, D.-W. Qu, J. Chen, C. Wu, F. Yang, W. Li, and G. Su, Bilayer $t-J-J_{\perp}$ model and magnetically mediated pairing in the pressurized nickelate $\text{La}_3\text{Ni}_2\text{O}_7$, *Phys. Rev. Lett.* **132**, 036502 (2024).
- [43] Y.-F. Yang, G.-M. Zhang, and F.-C. Zhang, Interlayer valence bonds and two-component theory for high- T_c superconductivity of $\text{La}_3\text{Ni}_2\text{O}_7$ under pressure, *Phys. Rev. B* **108**, L201108 (2023).
- [44] Y. Zhang, L.-F. Lin, A. Moreo, T. A. Maier, and E. Dagotto, Trends in electronic structures and s_{\pm} -wave pairing for the rare-earth series in bilayer nickelate superconductor $\text{R}_3\text{Ni}_2\text{O}_7$, *Phys. Rev. B* **108**, 165141 (2023).
- [45] D.-C. Lu, M. Li, Z.-Y. Zeng, W. Hou, J. Wang, F. Yang, and Y.-Z. You, Superconductivity from doping symmetric mass generation insulators: Application to $\text{La}_3\text{Ni}_2\text{O}_7$ under pressure, *arXiv:2308.11195* (2023).
- [46] Y.-H. Tian, Y. Chen, J.-M. Wang, R.-Q. He, and Z.-Y. Lu, Correlation effects and concomitant two-orbital s_{\pm} -wave superconductivity in $\text{La}_3\text{Ni}_2\text{O}_7$ under high pressure, *arXiv:2308.09698* (2023).
- [47] S. Rye, N. Witt, and T. O. Wehling, Quenched pair breaking by interlayer correlations as a key to superconductivity in $\text{La}_3\text{Ni}_2\text{O}_7$, *arXiv:2310.17465* (2024).
- [48] J. Huang, Z. D. Wang, and T. Zhou, Impurity and vortex states in the bilayer high-temperature superconductor $\text{La}_3\text{Ni}_2\text{O}_7$, *Phys. Rev. B* **108**, 174501 (2023).
- [49] R. Jiang, J. Hou, Z. Fan, Z.-J. Lang, and W. Ku, Pressure driven fractionalization of ionic spins results in cuprate-like high- T_c superconductivity in $\text{La}_3\text{Ni}_2\text{O}_7$, *Phys. Rev. Lett.* **132**, 126503 (2024).
- [50] Z. Liao, L. Chen, G. Duan, Y. Wang, C. Liu, R. Yu, and Q. Si, Electron correlations and superconductivity in $\text{La}_3\text{Ni}_2\text{O}_7$ under pressure tuning, *Phys. Rev. B* **108**, 214522 (2023).
- [51] C. Lu, Z. Pan, F. Yang, and C. Wu, Interlayer-coupling-driven high-temperature superconductivity in $\text{La}_3\text{Ni}_2\text{O}_7$ under pressure, *Phys. Rev. Lett.* **132**, 146002 (2024).
- [52] H. Oh and Y.-H. Zhang, Type-II $t-J$ model and shared superexchange coupling from Hund's rule in superconducting $\text{La}_3\text{Ni}_2\text{O}_7$, *Phys. Rev. B* **108**, 174511 (2023).
- [53] Q. Qin and Y.-f. Yang, High- T_c superconductivity by mobilizing local spin singlets and possible route to higher T_c in pressurized $\text{La}_3\text{Ni}_2\text{O}_7$, *Phys. Rev. B* **108**, L140504 (2023).
- [54] H. Sakakibara, N. Kitamine, M. Ochi, and K. Kuroki, Possible high T_c superconductivity in $\text{La}_3\text{Ni}_2\text{O}_7$ under high pressure through manifestation of a nearly half-filled bilayer Hubbard model, *Phys. Rev. Lett.* **132**, 106002 (2024).
- [55] Y. Shen, M. Qin, and G.-M. Zhang, Effective bilayer model hamiltonian and density-matrix renormalization group study for the high- T_c superconductivity in $\text{La}_3\text{Ni}_2\text{O}_7$ under high pressure, *Chin. Phys. Lett.* **40**, 127401 (2023).
- [56] D. A. Shilenko and I. V. Leonov, Correlated electronic structure, orbital-selective behavior, and magnetic correlations in double-layer $\text{La}_3\text{Ni}_2\text{O}_7$ under pressure, *Phys. Rev. B* **108**, 125105 (2023).
- [57] W. Wú, Z. Luo, D.-X. Yao, and M. Wang, Superexchange and charge transfer in the nickelate superconductor $\text{La}_3\text{Ni}_2\text{O}_7$ under pressure, *Sci China Phys Mech Astron* **67**, 117402 (2024).
- [58] I. V. Leonov, Electronic structure and magnetic correlations in trilayer nickelate superconductor $\text{La}_4\text{Ni}_3\text{O}_{10}$ under pressure, *arXiv:2401.07350* (2024).
- [59] J.-X. Wang, Z. Ouyang, R.-Q. He, and Z.-Y. Lu, Non-Fermi liquid and Hund correlation in $\text{La}_4\text{Ni}_3\text{O}_{10}$ under high pressure, *Phys. Rev. B* **109**, 165140 (2024).
- [60] Y. Zhang, L.-F. Lin, A. Moreo, T. A. Maier, and E. Dagotto, Prediction of s_{\pm} -wave superconductivity enhanced by electronic doping in trilayer nickelates $\text{La}_4\text{Ni}_3\text{O}_{10}$ under pressure, *arXiv:2402.05285* (2024).
- [61] P.-F. Tian, H.-T. Ma, X. Ming, X.-J. Zheng, and H. Li, Effective model and electron correlations in trilayer nickelate superconductor $\text{La}_4\text{Ni}_3\text{O}_{10}$, *arXiv:2402.02351* (2024).
- [62] X. Chen, J. Zhang, A. S. Thind, S. Sharma, H. LaBollita, G. Peterson, H. Zheng, D. P. Phelan, A. S. Botana, R. F.

- Klie, and J. F. Mitchell, Polymorphism in the Ruddlesden–Popper nickelate $\text{La}_3\text{Ni}_2\text{O}_7$: Discovery of a hidden phase with distinctive layer stacking, *J. Am. Chem. Soc.* **146**, 3640 (2024).
- [63] P. Puphal, P. Reiss, N. Enderlein, Y.-M. Wu, G. Khal-iullin, V. Sundaramurthy, T. Priessnitz, M. Knauff, L. Richter, M. Isobe, P. A. van Aken, H. Takagi, B. Keimer, Y. E. Suyolcu, B. Wehinger, P. Hansmann, and M. Hepting, Unconventional crystal structure of the high-pressure superconductor $\text{La}_3\text{Ni}_2\text{O}_7$, *arXiv:2312.07341* (2023).
- [64] H. Wang, L. Chen, A. Rutherford, H. Zhou, and W. Xie, Long-range structural order in a hidden phase of Ruddlesden–Popper bilayer nickelate $\text{La}_3\text{Ni}_2\text{O}_7$, *Inorg. Chem.* **63**, 5020 (2024).
- [65] G. H. Lander, P. J. Brown, J. Spal/ek, and J. M. Honig, Structural and magnetization density studies of La_2NiO_4 , *Phys. Rev. B* **40**, 4463 (1989).
- [66] J. Rodriguez-Carvajal, M. T. Fernandez-Diaz, and J. L. Martinez, Neutron diffraction study on structural and magnetic properties of La_2NiO_4 , *J. Condens. Matter Phys.* **3**, 3215 (1991).
- [67] J. Zhang, H. Zheng, Y.-S. Chen, Y. Ren, M. Yonemura, A. Huq, and J. F. Mitchell, High oxygen pressure floating zone growth and crystal structure of the metallic nickelates $\text{R}_4\text{Ni}_3\text{O}_{10}$ ($\text{R} = \text{La}, \text{Pr}$), *Phys. Rev. Mater.* **4**, 083402 (2020).
- [68] P. Blaha, K. Schwarz, F. Tran, R. Laskowski, G. K. H. Madsen, and L. D. Marks, WIEN2k: An APW+lo program for calculating the properties of solids, *J. Chem. Phys.* **152**, 074101 (2020).
- [69] A. A. Mostofi, J. R. Yates, G. Pizzi, Y.-S. Lee, I. Souza, D. Vanderbilt, and N. Marzari, An updated version of wannier90: A tool for obtaining maximally-localised Wannier functions, *Comput. Phys. Commun.* **185**, 2309 (2014).
- [70] J. Kunes, R. Arita, P. Wissgott, A. Toschi, H. Ikeda, and K. Held, Wien2wannier: From linearized augmented plane waves to maximally localized Wannier functions, *Comput. Phys. Commun.* **181**, 1888 (2010).
- [71] M. E. Merkel, A. Carta, S. Beck, and A. Hampel, solid_dmft: gray-boxing DFT+DMFT materials simulations with TRIQS, *J. Open Source Softw.* **7**, 4623 (2022).
- [72] O. Parcollet, M. Ferrero, T. Ayral, H. Hafermann, I. Krivenko, L. Messio, and P. Seth, TRIQS: A toolbox for research on interacting quantum systems, *Comput. Phys. Commun.* **196**, 398 (2015).
- [73] P. Seth, I. Krivenko, M. Ferrero, and O. Parcollet, TRIQS/CTHYB: A continuous-time quantum Monte Carlo hybridisation expansion solver for quantum impurity problems, *Comput. Phys. Commun.* **200**, 274 (2016).
- [74] J. Mravlje, M. Aichhorn, T. Miyake, K. Haule, G. Kotliar, and A. Georges, Coherence-incoherence crossover and the mass-renormalization puzzles in Sr_2RuO_4 , *Phys. Rev. Lett.* **106**, 096401 (2011).
- [75] X. Wang, M. J. Han, L. de’ Medici, H. Park, C. A. Marianetti, and A. J. Millis, Covalency, double-counting, and the metal-insulator phase diagram in transition metal oxides, *Phys. Rev. B* **86**, 195136 (2012).
- [76] H. Park, A. J. Millis, and C. A. Marianetti, Total energy calculations using DFT+DMFT: Computing the pressure phase diagram of the rare earth nickelates, *Phys. Rev. B* **89**, 245133 (2014).
- [77] A. Hampel, S. Beck, and C. Ederer, Effect of charge self-consistency in DFT + DMFT calculations for complex transition metal oxides, *Phys. Rev. Res.* **2**, 033088 (2020).
- [78] J. Karp, A. S. Botana, M. R. Norman, H. Park, M. Zingl, and A. Millis, Many-body electronic structure of NdNiO_2 and CaCuO_2 , *Phys. Rev. X* **10**, 021061 (2020).
- [79] M. Kitatani, L. Si, O. Janson, R. Arita, Z. Zhong, and K. Held, Nickelate superconductors—a renaissance of the one-band Hubbard model, *npj Quantum Mater.* **5**, 59 (2020).
- [80] H. LaBollita and A. S. Botana, Correlated electronic structure of a quintuple-layer nickelate, *Phys. Rev. B* **105**, 085118 (2022).
- [81] P. Worm, L. Si, M. Kitatani, R. Arita, J. M. Tomczak, and K. Held, Correlations tune the electronic structure of pentalayer nickelates into the superconducting regime, *Phys. Rev. Mater.* **6**, L091801 (2022).
- [82] S. J. Skinner, Characterisation of $\text{La}_2\text{NiO}_{4+\delta}$ using in-situ high temperature neutron powder diffraction, *Solid State Sciences* **5**, 419 (2003).
- [83] F. Lechermann, Assessing the correlated electronic structure of lanthanum nickelates, *Electronic Structure* **4**, 015005 (2022).
- [84] M.-C. Jung, J. Kapeghian, C. Hanson, B. Pamuk, and A. S. Botana, Electronic structure of higher-order Ruddlesden–Popper nickelates, *Phys. Rev. B* **105**, 085150 (2022).
- [85] H. Eisaki, S. Uchida, T. Mizokawa, H. Namatame, A. Fujimori, J. van Elp, P. Kuiper, G. A. Sawatzky, S. Hosoya, and H. Katayama-Yoshida, Electronic structure of $\text{La}_{2-x}\text{Sr}_x\text{NiO}_4$ studied by photoemission and inverse-photoemission spectroscopy, *Phys. Rev. B* **45**, 12513 (1992).
- [86] H. Li, X. Zhou, T. Nummy, J. Zhang, V. Pardo, W. E. Pickett, J. F. Mitchell, and D. S. Dessau, Fermiology and electron dynamics of trilayer nickelate $\text{La}_4\text{Ni}_3\text{O}_{10}$, *Nat. Commun* **8**, 704 (2017).
- [87] J. Zhang, D. Phelan, A. S. Botana, Y.-S. Chen, H. Zheng, M. Krogstad, S. G. Wang, Y. Qiu, J. A. Rodriguez-Rivera, R. Osborn, S. Rosenkranz, M. R. Norman, and J. F. Mitchell, Intertwined density waves in a metallic nickelate, *Nat. Commun* **11**, 6003 (2020).
- [88] F. Lechermann, S. Bötzel, and I. M. Eremin, Electronic instability, layer selectivity and Fermi arcs in $\text{La}_3\text{Ni}_2\text{O}_7$, *arXiv:2403.12831* (2024).
- [89] S. N. Abadi, K.-J. Xu, E. G. Lomeli, P. Puphal, M. Isobe, Y. Zhong, A. V. Fedorov, S.-K. Mo, M. Hashimoto, D.-H. Lu, B. Moritz, B. Keimer, T. P. Devereaux, M. Hepting, and Z.-X. Shen, Electronic structure of the alternating monolayer-trilayer phase of $\text{La}_3\text{Ni}_2\text{O}_7$, *arXiv:2402.07143* (2024).
- [90] Q.-G. Yang, K.-Y. Jiang, D. Wang, H.-Y. Lu, and Q.-H. Wang, Effective model and s_{\pm} -wave superconductivity in trilayer nickelate $\text{La}_4\text{Ni}_3\text{O}_{10}$, *arXiv:2402.05447* (2024).
- [91] Y. Zhang, L.-F. Lin, A. Moreo, T. A. Maier, and E. Dagotto, Electronic structure, self-doping, and superconducting instability in the alternating single-layer trilayer stacking nickelates $\text{La}_3\text{Ni}_2\text{O}_7$, *arXiv:2404.16600* (2024).
- [92] G. Kresse and J. Hafner, Ab initio molecular dynamics for liquid metals, *Phys. Rev. B* **47**, 558 (1993).
- [93] G. Kresse and J. Furthmüller, Efficient iterative schemes for ab initio total-energy calculations using a plane-wave basis set, *Phys. Rev. B* **54**, 11169 (1996).

- [94] G. Kresse and D. Joubert, From ultrasoft pseudopotentials to the projector augmented-wave method, [Phys. Rev. B **59**, 1758 \(1999\)](#).
- [95] J. P. Perdew, K. Burke, and M. Ernzerhof, Generalized gradient approximation made simple, [Phys. Rev. Lett. **77**, 3865 \(1996\)](#).
- [96] G. J. Kraberger, R. Triebl, M. Zingl, and M. Aichhorn, Maximum entropy formalism for the analytic continuation of matrix-valued Green's functions, [Phys. Rev. B **96**, 155128 \(2017\)](#).